



PAPER • OPEN ACCESS

# Trap induced broadening in a potential hydrogen lattice clock

To cite this article: J P Scott *et al* 2024 *Metrologia* **61** 025001

View the [article online](#) for updates and enhancements.

## You may also like

- [A comparison of the frequencies of the 1S-2S and 2S-4P transitions in atomic hydrogen](#)  
C D Thompson, G H Woodman, C J Foot et al.
- [Roadmap on photonic, electronic and atomic collision physics: II. Electron and antimatter interactions](#)  
Stefan Schippers, Emma Sokell, Friedrich Aumayr et al.
- [Observation of the 1S-2S transition in atomic hydrogen in an atomic beam](#)  
C J Foot, P Hannaford, D N Stacey et al.

# Trap induced broadening in a potential hydrogen lattice clock

J P Scott<sup>\*</sup> , R M Potvliege , D Carty  and M P A Jones 

Department of Physics, Durham University, Durham, United Kingdom

E-mail: [joseph.p.scott@durham.ac.uk](mailto:joseph.p.scott@durham.ac.uk)

Received 27 September 2023, revised 10 January 2024

Accepted for publication 12 January 2024

Published 30 January 2024



CrossMark

## Abstract

We consider the potential use of optical traps for precision measurements in atomic hydrogen (H). Using an implicit summation method, we calculate the atomic polarisability, the rates of elastic/inelastic scattering and the ionisation rate in the wavelength range (395–1000) nm. We extend previous work to predict three new magic wavelengths for the 1S–2S transition. At the magic wavelengths, the 1S–2S transition is unavoidably and significantly broadened due to trap-induced ionisation associated with the high intensity required to trap the 1S state. However, we also find that this effect is partially mitigated by the low mass of H, which increases the trap frequency, enabling Lamb–Dicke confinement in shallow lattices. We find that a H optical lattice clock, free from the motional systematics which dominate in beam experiments, could operate with an intrinsic linewidth of the order of 1 kHz. Trap-induced losses are shown not to limit measurements of other transitions.

Keywords: hydrogen spectroscopy, optical lattice clock, precision measurement

## 1. Introduction

Fundamental physics tests in hydrogen [1–5] rely on determining two parameters; the Rydberg constant  $R_\infty$ , which relates the theoretical energy scale to the SI system of units, and the ‘size’ of the proton, characterized by its charge radius  $r_p$ , which cannot yet be accurately calculated from quantum chromodynamics [6]. The 1S–2S transition frequency, which has been measured with a fractional uncertainty of  $\sim 10^{-15}$  [7, 8], can be used to precisely determine one of these parameters, but must be complemented by measurements of other transitions or scattering-based measurements of  $r_p$  [9]. It is well-known that the current dataset of relevant measurements is internally inconsistent [10, 11], and inconsistent with measurements in muonic hydrogen [12]; a problem often called the ‘proton charge radius puzzle’ [13]. Whilst this variation may

be evidence of new physics (e.g. a hidden sector, light scalar boson [4, 5, 14]), the disagreement between two recent measurements of the 1S–3S transition [15, 16] indicate that experimental systematics are at least partially responsible.

Currently, all precision H spectroscopy experiments rely on an atomic beam as the source [7, 8, 14–21]. Line shifts and broadening due to motional (Doppler) effects are a significant source of uncertainty, and careful velocity filtering [7] and/or lineshape analysis (see the supplementary information of [14]) is required to extract precise measurements of the transition frequency. As a result, the overall uncertainty in measurements of the 1S–2S transition has not significantly advanced in 10 years, and motional effects may be a significant source of inconsistency within the H world dataset.

In contrast, the precision spectroscopy of heavier neutral atoms has been revolutionised by the use of ultra-cold *trapped* atoms in optical lattice clocks (OLCs) [22–26]. Here atoms are confined in a ‘magic wavelength’ optical lattice such that trap-induced lineshifts cancel, and motional effects are eliminated by operating in the tight confinement (Lamb–Dicke) regime [22]. OLCs have now reached a precision of  $\sim 10^{-18}$ , which surpasses the current definition of the SI second [27]. An anti-hydrogen ( $\bar{\text{H}}$ ) lattice clock operating on the 1S–2S

\* Author to whom any correspondence should be addressed.



Original Content from this work may be used under the terms of the [Creative Commons Attribution 4.0 licence](https://creativecommons.org/licenses/by/4.0/). Any further distribution of this work must maintain attribution to the author(s) and the title of the work, journal citation and DOI.

was recently proposed [28]; comparing H and  $\bar{H}$  clocks would provide a stringent test of CPT symmetry [29–32].

A magic wavelength for the 1S–2S transition has already been established [33, 34]. However scattering of the trapping light can also lead to decoherence via heating, inelastic scattering and ionization. Heating from elastic scattering is known to be small [28]. Inelastic cross-sections have been calculated for some wavelengths and final states [35–37], alongside two-photon ionization rates from the 2S state [36, 38–42], but so far these have not been discussed in the context of precision measurement with optically trapped H atoms.

In this paper we give a comprehensive treatment of the effect of trap-induced scattering and multi-photon ionisation on measurements involving the 2S state of H. We pay special attention to rates at four 1S–2S magic wavelengths—one known and three newly reported. We find excellent agreement with existing calculations and extend these works to consider all relevant final states. At trap intensities relevant to the operation of an OLC, we find that two-photon ionisation provides the dominant loss channel. The result is a considerable reduction in the 2S lifetime and the achievable linewidth therefore remains similar to atomic beam experiments. However we show that it remains possible to reach the Lamb–Dicke regime, eliminating motional effects up to a small relativistic Doppler shift. An OLC could therefore test our understanding of systematic uncertainties in the H dataset at a level relevant to the proton radius puzzle. For transitions to higher-lying states (e.g. Rydberg states), the additional broadening no longer limits the coherence time, and atoms trapped in an optical tweezer array, for example, could be useful for eliminating uncertainties due to long-range interactions.

All mathematical expressions are given in atomic units (see e.g. [43]).

## 2. Numerical calculations

Central to any OLC is the optical lattice; a one dimensional lattice is described by the potential [44]:

$$U(x) = U_0 \cos^2 kx, \quad (1)$$

with

$$U_0 = -2\pi\alpha_{\text{FS}}\alpha_a(\omega)I_0, \quad (2)$$

where  $k$  and  $\omega$  are the wave number and frequency of the lattice light respectively,  $I_0$  is the peak lattice intensity,  $\alpha_{\text{FS}}$  is the fine structure constant, and  $\alpha_a$  is the polarisability of atomic state  $a$ . Throughout the text, we assume that the lattice light is linearly polarised in the  $\hat{z}$  direction and that this matches the atomic axis of quantisation. It is often useful to characterise the depth of the lattice  $|U_0|$  in terms of the single lattice photon recoil energy,  $E_{\text{rec}} = \omega^2\alpha_{\text{FS}}^2/2m_{\text{H}}^1$ , giving a dimensionless lattice depth  $D = |U_0|/E_{\text{rec}}$ .

<sup>1</sup> This definition (in atomic units) is equivalent to  $E_{\text{rec}} = \hbar^2 k^2 / 2m_{\text{H}}$ .

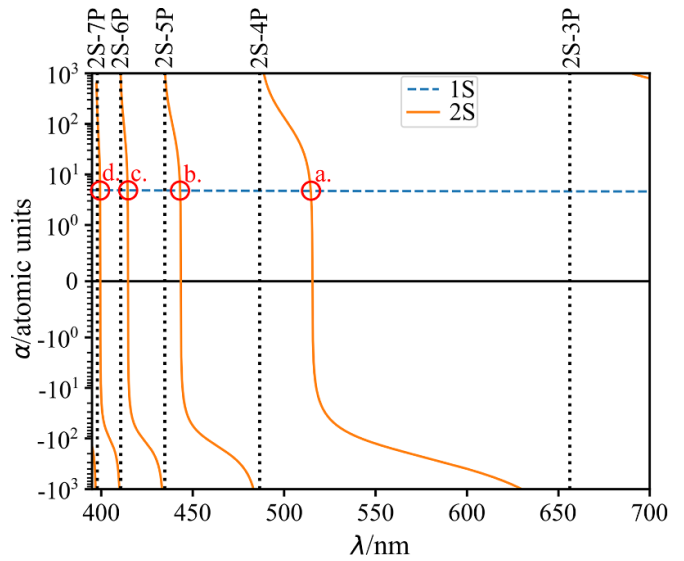


**Figure 1.** Polarisability of the 1S (blue dashed line) and 2S states (solid orange line) versus wavelength. A symmetric log scale is used on the y-axis. The four magic wavelengths listed in table 1. are labelled as (a)–(d). Vertical dotted lines indicate 2S– $n$ P atomic resonances.

The polarisability of state  $a$  with zero orbital angular momentum,  $l=0$  ( $n$ S state) at frequency  $\omega$  is given by [45, 46],

$$\alpha_a(\omega) = \frac{1}{3} \sum_k \left( \frac{|r_{ka}|^2}{\omega_{ka} - \omega} + \frac{|r_{ka}|^2}{\omega_{ka} + \omega} \right). \quad (3)$$

The sum is across all states  $k$  that are dipole coupled to  $a$ . Here  $r_{ka}$  are the radial dipole matrix elements as defined in appendix A (equation (A5)) and  $\omega_{ka} = \omega_k - \omega_a$  is the difference in energy between the states  $k$  and  $a$ .

We calculate the atomic polarisability using the implicit summation method described in appendix B. The calculation is non-relativistic. The leading order corrections to these values come from relativistic and field configuration terms and are of the order of  $\sim\alpha_{\text{FS}}^2$  [33, 34]. Therefore values reported in this paper are quoted up to four significant figures. The polarisability of the 1S and 2S states is plotted for a range of optical wavelengths in figure 1.

Magic wavelengths, where the polarisability of both states is equal, are critical for an OLC as they eliminate the differential light shift on the clock transition. To find these wavelengths, we numerically solve  $|\alpha_{2\text{S}}(\omega) - \alpha_{1\text{S}}(\omega)| = 0$  in the region around each intersection labelled a–d in figure 1. We find four magic wavelengths in the considered range<sup>2</sup> at 514.6 nm, 443.2 nm, 414.5 nm, and 399.5 nm. The polarisability at the magic wavelengths are reported in table 1.

Figure 1 and table 1 show that the polarisability at the magic wavelength is very small, approximately 4.8 atomic

<sup>2</sup> For comparison it is useful to give these to more significant figures: 514.6464 nm, 443.212 nm, 414.483 nm, and 399.451 nm. The first agrees very well with the literature [33, 34].

**Table 1.** Key parameters for 1S-2S spectroscopy in magic wavelength traps: polarisability  $\alpha$  (in atomic units) of both states and the intensity that produces a  $1E_{\text{rec}}$  deep lattice. Values for the Rayleigh scattering rate  $R_{\text{el}}$ , the Raman scattering rate  $R_{\text{in}}$  and the two-photon ionisation rate  $R_{\text{ion}}$  are stated at a depth of  $1 E_{\text{rec}}$ .

$\lambda/\text{nm}$	$\alpha$	$I/\text{MW cm}^{-2}$	$R_{\text{el}}/\text{s}^{-1}$	$R_{\text{in}}/\text{s}^{-1}$	$R_{\text{ion}}/\text{s}^{-1}$
514.6	4.730	3.372	$7.986 \times 10^{-3}$	61.49	32.19
443.2	4.813	4.460	$17.16 \times 10^{-3}$	69.41	30.29
414.5	4.863	5.056	$24.23 \times 10^{-3}$	73.90	29.04
399.5	4.890	5.413	$29.31 \times 10^{-3}$	76.78	28.33

units compared to  $\sim 280$  atomic units in Sr at the 813 nm magic wavelength [47], due to the absence of 1S resonances at wavelengths shorter than 121.6 nm (the Lyman alpha line). In addition, the low mass of H leads to large recoil velocities at optical frequencies and substantial laser power is required to trap in the 1S state. OLCs usually operate in deep optical traps, often around  $100E_{\text{rec}}$ . Such a deep lattice for a hydrogen OLC requires intensities of  $100$ 's  $\text{MW cm}^{-2}$  (see table 1), on the order of  $10^4$  (written as  $O(10^4)$ ) times larger than a comparable lattice for Sr. Nevertheless, such high intensities are achievable with current laser technology, particularly for 514.6 nm where significant power is available from frequency-doubled 1029.2 nm radiation [28, 48].

A major concern in optical trapping is off-resonant atom-photon scattering. It is useful to separate the various scattering processes by the final internal state of the atom. Firstly we consider elastic or Rayleigh scattering. The key effect of elastic scattering is to change the vibrational state of trapped atoms, resulting in heating [44]. The elastic scattering rate is closely related to the polarisability and can be written as (see appendix A)

$$R_{\text{el}} = \omega^3 \alpha_{\text{FS}}^4 \frac{8\pi}{3} |\alpha_a(\omega)|^2 I. \quad (4)$$

This rate is the same for both the 1S and 2S states in a magic wavelength trap. Therefore, we present a single value for the elastic scattering rate in table 1. These rates are very small, only approaching the spontaneous decay rate at around  $1000E_{\text{rec}}$  at 514.6 nm ( $270E_{\text{rec}}$  at 399.5 nm).

Next, we consider inelastic scattering to other bound internal states. Critically, this includes scattering directly to the ground state. As explained in appendix A, the scattering rate from an initial S state  $a$  to final state(s)  $b$  of energy  $\omega_b$  can be expressed in the following form:

$$R_{ba} = \omega_s^3 \alpha_{\text{FS}}^4 \mathcal{A}_{ba} \left[ \sum_k \left( \frac{r_{bk}r_{ka}}{\omega_{ka} \mp \omega} + \frac{r_{bk}r_{ka}}{\omega_{bk} \pm \omega} \right) \right]^2 I, \quad (5)$$

where  $\omega_s = -\omega_{ba} \pm \omega$  is the angular frequency of the scattered photon and  $\mathcal{A}_{ba}$  is an angular factor. Dipole selection rules restrict scattering to only S or D final states. Upper and lower signs relate to Raman scattering (RS) and singly stimulated two-photon emission (SSTPE) [49] respectively. A breakdown of the total 2S inelastic scattering rate according to final  $n, l$  state (summing over magnetic quantum number  $m_b$ ) is given in table 2 and indicates that inelastic scattering to the ground state is the dominant process.

The scattering rates were calculated with the same implicit summation method as the polarisability (appendix B). The elastic scattering rate is consistent with existing work [36, 50], while results for scattering to 1S, 3S and 3D states at 514.6 nm are in good agreement with previous calculations close to this value [36]. The results for additional final states and other magic wavelengths are new, to the best of our knowledge. Leading order corrections from relativistic and field configuration terms are of the same order as for the polarisability.

The total inelastic scattering rate is given by the sum of RS and SSTPE rates for all allowed final states  $R_{\text{in}} = \sum_{b \neq a}^{\omega_{ba} < \omega} R_{ba}$ . These total inelastic scattering rates are presented in table 1 and are much larger than the corresponding elastic scattering rates, exceeding the rate of spontaneous decay for depths as low as  $O(0.1)E_{\text{rec}}$ .

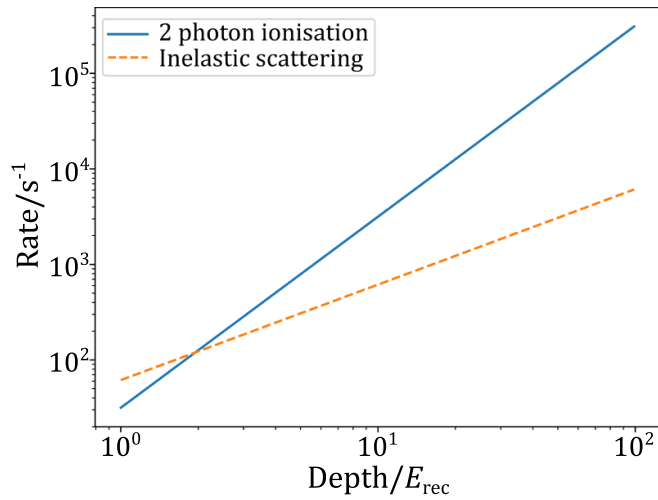
Lastly we consider ionisation. Single photon ionisation from the 2S state is only possible at wavelengths below 365 nm. Ionisation at the magic wavelengths thus involves absorption of at least two photons. We use the STRFLO program [51] to calculate multi-photon ionisation rates. The ionisation rates at the magic wavelengths are given in the final column of table 1 for  $D=1$ . Inelastic scattering rates scale linearly with intensity, while these ionisation rates scale with intensity squared. Therefore, ionisation quickly dominates inelastic scattering as trap depth increases past  $O(1)E_{\text{rec}}$ , as shown in figure 2. The dominance of ionisation for relatively low trap depths is a result of the low polarisability of the 1S state, and the high trapping intensities that result.

Table 1 and figure 2 indicate that at magic wavelengths, the impact of trap induced ionisation is enormous. At a depth of  $1 E_{\text{rec}}$  the 2S state lifetime is reduced from 125 ms to  $O(10)$  ms, while at  $100E_{\text{rec}}$  it becomes just  $O(1)$   $\mu\text{s}$ . These results impose severe limitations on the coherence times that can be achieved in a H lattice clock.

The impact of operating at a magic wavelength is highlighted by plotting the scattering and ionisation rates as a function of wavelength, as in figure 3. In figure 3(a) the rates are shown for a constant intensity of  $100 \text{MW cm}^{-2}$ ; corresponding to trap depths ranging from  $30E_{\text{rec}}$  at 514.6 nm to  $18E_{\text{rec}}$  at 399.5 nm. Here, peaks in the rates correspond to the resonances of the Balmer series. Two-photon ionisation does not extend past the threshold at 729 nm. For longer wavelengths, ionisation proceeds via the absorption of at least three photons. The 3-photon ionisation rates vary as  $I^3$  but are generally much smaller than the inelastic scattering rate at these intensities, except at narrow 2 photon resonances with intermediate bound states.

**Table 2.** Rates for allowed inelastic scattering processes with nS and nD final states (listed according to final state) and total inelastic scattering rates for the 2S initial states. The rates are given per unit depth in units of  $s^{-1}$  at a depth of  $1E_{\text{rec}}$  in the 2S state.

$\lambda/\text{nm}$	1S	3S	3D	4S	4D	5S	5D	6S	6D	$R_{\text{in}}/D$
514.6	57.32	3.843	0.3329	—	—	—	—	—	—	61.49
443.2	62.85	3.269	0.1861	2.295	0.8110	—	—	—	—	69.41
414.5	65.75	3.249	0.1570	1.892	0.5481	1.467	0.8388	—	—	73.90
399.5	67.53	3.272	0.1453	1.802	0.4636	1.207	0.6109	1.005	0.7460	76.78



**Figure 2.** Comparison between the two-photon ionisation rate (solid blue lines) and the inelastic scattering rate (dashed orange lines) for varying trap depth at 514.6 nm. At this scale, these plots look the same for all magic wavelengths. The intersection between the two lines does not change substantially either: it is at  $2E_{\text{rec}}$  for 514.6 nm and  $3.2E_{\text{rec}}$  for 399.5 nm.

In contrast, figures 3(b) and (c) show the rates at a constant trap depth  $D = 100$ . In (b) it is the 2S trap depth that is fixed, while in (c) it is the 1S trap depth. We note that  $D$  ignores the sign of the potential; in wavelength regions where the polarisability is negative (blue detuned) atoms are trapped at intensity minima and the actual loss rate observed in experiment may be lower. Compared to figures 3(a) and (b) shows an extra series of divergences in the inelastic scattering and 2-photon ionisation rates. These originate from zero-crossings of the 2S polarisability. Here the intensity required to produce a trap at a given depth, and hence the rates, diverge. The magic wavelengths sit very close to these zero-crossings, suppressing elastic scattering, but enhancing inelastic scattering and ionisation at a given trap depth. The 1S polarisability is essentially flat in this region and does not cross zero, so the shape of figure 3(c) is very similar to part (a). Compared to part (b) the rates are generally much larger, except at the magic wavelength. Again, this is a result of the small, almost constant, polarisability of the 1S state.

### 3. Discussion

First, we consider a 1S–2S hydrogen OLC, operating in a magic wavelength lattice. As seen in the previous section, the

lifetime  $\tau$  of the 2S state is severely reduced by two-photon ionisation at these wavelengths. This broadens the minimal linewidth of the 1S–2S transition,  $\Gamma_{\text{FWHM}} = 1/(2\pi\tau)$ . This effect is considerable in the deep lattices that are usual for OLCs. For example, in a  $100E_{\text{rec}}$  deep magic wavelength lattice, the 1S–2S line is broadened from a natural width of 1.27 Hz to an ionisation dominated  $\sim 50$  kHz.

An important motivation for using lattice-trapped atoms is the potential to eliminate the velocity dependence of the lineshape. To achieve this we must operate in the limit of resolved sidebands, where the trap frequency (given in SI units),

$$\nu_{\text{T}} = \sqrt{D} \frac{h}{m_{\text{H}} \lambda^2}, \quad (6)$$

is much larger than the linewidth,  $\nu_{\text{T}} \gg \Gamma_{\text{FWHM}}$ . In this limit, the effects of changes in vibrational state are separated into distinct sideband signals. This leaves a central carrier line that is insensitive to motional effects and symmetric in the non-relativistic limit. The low mass of H and relatively short magic wavelengths result in large trap frequencies,  $\approx \sqrt{D} \times 2$  MHz. This compares favourably with the linewidth and makes it simple to achieve well-resolved sidebands. In fact, the broadened linewidth only becomes comparable to the trap frequencies for depths greater than<sup>3</sup>  $O(1000)E_{\text{rec}}$ .

It is also desirable to operate a clock in the Lamb–Dicke regime, where the separation of vibrational states is much larger than the recoil energy of a 243 nm probe photon,  $h\nu_{\text{T}} \gg E_{\text{probe}}$ . This suppresses transitions to other vibrational states and reduces the relative size of the sideband signals compared to the carrier. Whilst the Doppler-free driving of the 1S–2S transition at 243 nm suppresses first order changes in momentum, higher-order effects due to wavefront curvature remain. These momentum-changing effects appear in the second-order sidebands (see appendix C). To make a quantitative statement, we demand that the probability of remaining in the ground vibrational state  $P_{n=0 \rightarrow n=0} > 0.9$  (equivalent to  $\eta^2 < 0.381$ ), and find the results listed in table 3. We note that the carrier remains subject to a small second-order Doppler shift arising from time dilation [52]. Following the calculation of [53], we obtain a fractional frequency shift of  $-9.68 \times 10^{-18}$  in the vibrational ground state (for  $\nu_{\text{T}} = 8.79$  MHz) which corresponds to an absolute shift of  $-23.9$  mHz in the 1S–2S transition frequency (see appendix C). Similar

<sup>3</sup> Or for depths lower than  $O(10^{-11})E_{\text{rec}}$ , but this is smaller than the minimum trap depth against gravity.

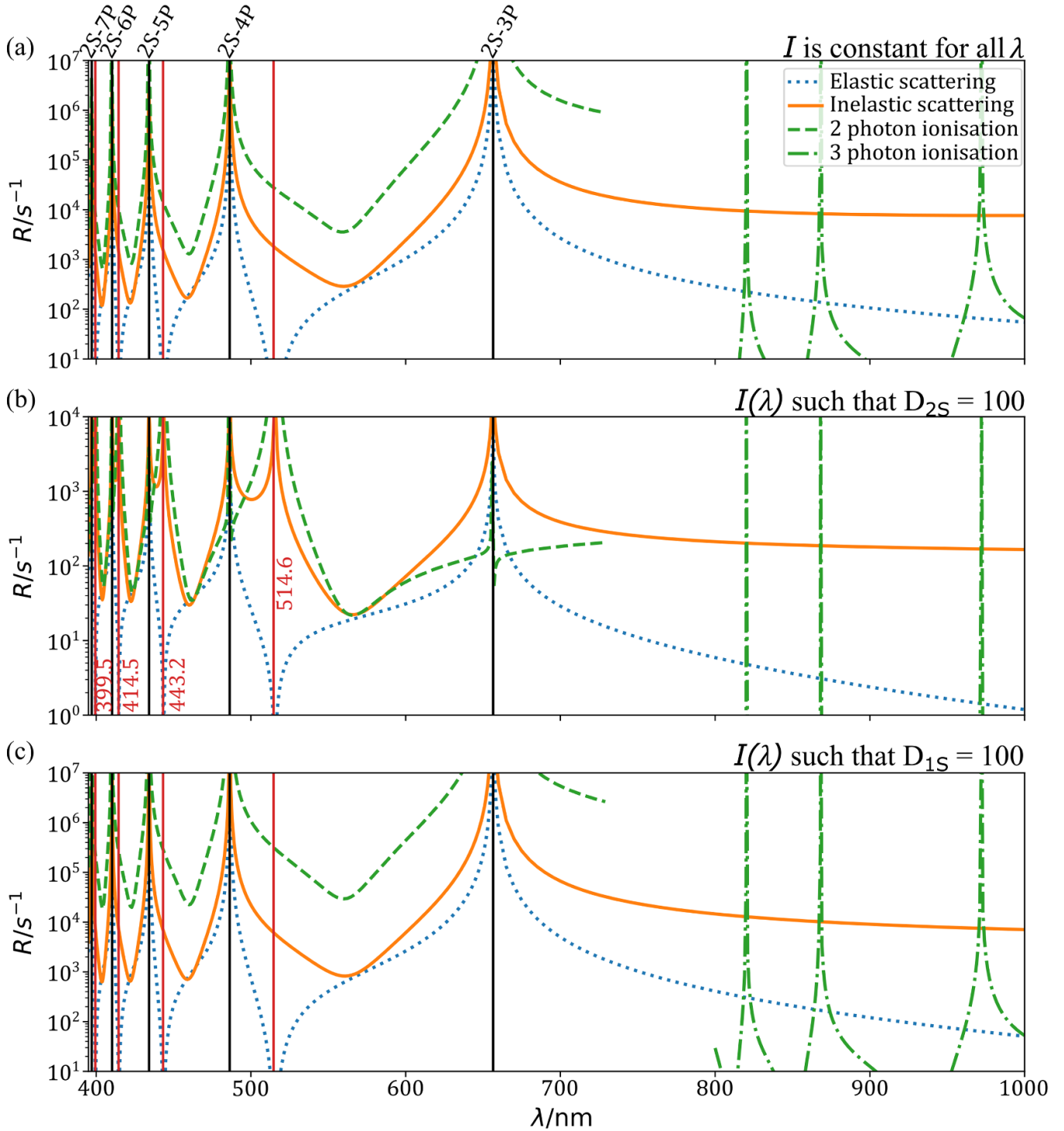


**Figure 3.** The variation of elastic scattering (dotted blue lines), inelastic scattering (solid orange lines), and two-photon ionisation (dashed green lines) rates from the 2S state across a range of wavelengths. The line showing two photon ionisation only extends to the threshold. Also plotted are the three-photon ionisation rates (dashdotted lines) for wavelengths (800–1000) nm, which is the leading order ionisation process in this region. (a) Rates at constant intensity  $I = 100 \text{ MWcm}^{-2}$ . (b) and (c) rates at variable intensities which maintain a constant  $D = 100$  lattice for depths defined with reference to the 2S and 1S states respectively. Black vertical lines indicate 2S atomic resonances and red vertical lines indicate magic wavelengths.

calculations for thermal vibrational states result in a fractional shift of  $O(10^{-17})$ , which is still well below the current uncertainty in the 1S–2S measurement [7].

It is instructive to compare the results in table 3 to measurements in cold atomic beams [7, 8]. The systematic uncertainty in beam measurements is dominated by velocity-dependent

**Table 3.** The trap depth and 1S–2S linewidth at the intensity where the Lamb–Dicke constraint is met for each magic wavelength. These depths all relate to trap frequencies of 8.79 MHz and a Lamb–Dicke parameter of  $\eta^2 = 0.381$ .

$\lambda/\text{nm}$	$(\mu_T/\sqrt{D})/\text{MHz}$	$D$	$\Gamma_{\text{FWHM}}/\text{kHz}$
514.6	1.50	34.5	6.43
443.2	2.02	19.0	1.95
414.5	2.31	14.5	1.14
399.5	2.48	12.5	0.857

effects such as the second-order Doppler shift. To reduce these effects, the measurement must selectively address atoms that sit within a very narrow range in the slow tail of the velocity distribution. This results in a momentum-dependent asymmetric lineshape with a measured width of  $\sim 2$  kHz [7]. The linewidths in table 3 are comparable, with the significant advantage that the lineshape is symmetric and no longer velocity dependent.

One area where a trapped-atom measurements often lose out is statistics, due to the reduced duty cycle and atom number associated with cooling and trapping. In Sr OLCs, statistical power is improved by reading out fluorescence from a fast-cycling transition out of the ground state [22]. Unfortunately, due to the lack of laser power at Lyman series wavelengths [54], such a scheme is impractical in H. At the magic wavelength, trap-induced ionisation will provide a continuous readout of the 2S state population, with the drawback that it is destructive and so the trap must be replenished. Currently, cooling and loading atomic H into an optical trap is an open problem, but it is clear that optimising the experimental duty cycle will be crucial in minimising the statistical uncertainty that can be achieved.

An alternative to working at a magic wavelength is to move to longer wavelengths where two-photon ionisation is suppressed<sup>4</sup>. However, using a non-magic trap introduces intensity-dependent systematics to the measurement exacerbated by the large differential light shift across the transition (e.g. the 2S polarisability is around 40 times larger than the 1S polarisability at 1064 nm). Also, the need to trap atoms in the 1S state as well as the 2S state means broadening from inelastic scattering is still significant (compare figures 3(b) and (c)). In addition, the lower trap frequencies available at long wavelengths compared to the magic wavelengths mean that even deeper traps are required to enter the Lamb–Dicke regime.

However, the 2S state provides a suitable spectroscopic ground state with accessible transitions to many states of higher principal quantum number  $n$  (e.g. [14, 17, 18, 21]). Transitions to high-lying Rydberg states are particularly interesting in the context of a trapped atom measurement [4]. The well-defined inter-atomic spacing of a lattice or tweezer array

enables control of strong dipole–dipole interactions. It is not necessary to trap at a 1S–2S magic wavelength, so one can trap with much lower intensities at wavelengths with larger 2S polarisability. This significantly reduces the rates of two-photon ionisation and inelastic scattering for traps at a given depth (see figure 3(b)). For example, even a very deep trap of  $D = 100$  (for the 2S state) only quenches the 2S lifetime to  $\sim 6$  ms at 1000 nm. Further, higher lying states are generally short-lived: low- $n$  states with lifetimes of  $O(10)$  ns [55], whilst high-lying states can have lifetimes of 100's  $\mu\text{s}$  [56, 57]. In this case, the reduced lifetime the 2S state does not limit the measured linewidth which is instead dominated by the natural lifetime of the high-lying state.

Finally, we mention the implications for measurements in deuterium (D) and  $\bar{\text{H}}$ . First, the non-relativistic theory of H and D is identical up to a difference in the reduced mass,  $\mu$ , of  $(\mu_{\text{D}} - \mu_{\text{H}})/\mu_{\text{H}} = 2.702 \times 10^{-4}$ . Thus the conclusions drawn for H are valid for D, with relative differences in exact values  $O(10^{-4})$ . The structure of H and  $\bar{\text{H}}$  are identical. As such, the results presented in this paper also hold for  $\bar{\text{H}}$  with the same level of precision.

## 4. Conclusions

We have calculated the polarisability of the 1S and 2S states in atomic hydrogen and identified new magic wavelengths in the range (395–1000) nm (figure 1). We have also calculated the atom-photon scattering and two-photon ionisation rates out of the 2S state in this wavelength range (figure 3), paying particular attention to rates at the magic wavelengths (tables 1 and 2).

Two-photon ionisation significantly broadens the 1S–2S transition linewidth in deep magic wavelength traps. This broadening is a consequence of the low polarisability of the 1S state and the resultant high trapping intensities. However, the low mass of atomic hydrogen allows for high trap frequencies. This makes it possible to enter the resolved sideband and Lamb–Dicke regimes in relatively shallow traps compared to heavier atoms like Sr (see table 3), opening a route to spectroscopy free from momentum-dependent systematics. In these shallower traps, the effect of ionisation is no longer catastrophic, and linewidths of  $\sim 1$  kHz are achievable, especially at the shorter magic wavelengths.

It is unlikely that a 1S–2S lattice clock will be competitive as an absolute frequency reference when compared to Sr lattice clocks or modern ion clocks. It could offer a measurement of the 1S–2S transition in H, D and even  $\bar{\text{H}}$  with a narrow line, free from velocity-dependent systematics. Such a measurement provides a litmus test for unrecognised velocity-dependent systematics in the current H data set. Further, comparisons between clock measurements in H, D, and  $\bar{\text{H}}$  would set powerful constraints on possible physics beyond the Standard Model [58] and test CPT symmetry [29–32].

The reduced lifetime of the 2S state does not limit spectroscopy to higher-lying states in the same way, as the

<sup>4</sup> The Lamb shift implies that a very long magic wavelength should exist between the 2S–3P and the 2S–2P<sup>1/2</sup>/2P<sup>3/2</sup> resonances, but this cannot be obtained by the non-relativistic theory alone.

excited-state lifetimes are already short. Therefore trapped atom spectroscopy is promising for transitions to Rydberg states where a well-defined spacing becomes essential. Experiments aiming to produce optically trapped cold H atoms for precision spectroscopy are now underway in several groups [59, 60], providing exciting perspectives for the future

## Acknowledgments

J P Scott is supported by a Stubbs Scholarship, and we gratefully thank Rodney and Frances Stubbs for their support. We thank Dylan Yost and Thomas Udem for useful comments and advice.

## Appendix A. Scattering rates

The differential cross section for the emission of a scattered photon in the solid angle  $d\Omega$  is given by the Kramers–Heisenberg formula [61]:

$$\frac{d\sigma}{d\Omega} = \sum_b^{\omega_{ba} < \omega} \sum_{s=1,2} \omega (\pm\omega - \omega_{ba})^3 \alpha_{\text{FS}}^4 \times \left| \sum_k \left( \frac{\epsilon_s^* \cdot \mathbf{r}_{bk} \epsilon \cdot \mathbf{r}_{ka}}{\omega_{ka} \mp \omega} + \frac{\epsilon \cdot \mathbf{r}_{bk} \epsilon_s^* \cdot \mathbf{r}_{ka}}{\omega_{kb} \pm \omega} \right) \right|^2, \quad (\text{A1})$$

where  $\mathbf{r}_{ka}$  is the dipole matrix element  $\langle k | \mathbf{r} | a \rangle$ ,  $\omega_{ka} = \omega_k - \omega_a$ ,  $\epsilon$  is the polarisation vector of the trap photon—taken to be linear—and  $\epsilon_1$  and  $\epsilon_2$  are two orthogonal unit vectors spanning the plane orthogonal to the direction of emission of the scattered photon. For emission in the direction of co-latitude angle  $\vartheta$  and azimuthal angle  $\varphi$ , these two orthogonal vectors could be chosen, e.g. as having polar angles  $\vartheta_1 = \vartheta - \pi/2$  and  $\varphi_1 = \varphi$  for  $\epsilon_1$  and  $\vartheta_2 = \pi/2$  and  $\varphi_2 = \varphi - \pi/2$  for  $\epsilon_2$ . Given this differential cross section, the total scattering rate is obtained as

$$R = \int d\Omega \frac{d\sigma}{d\Omega} \frac{I}{\omega} = \sum_b^{\omega_{ba} < \omega} R_{ba}, \quad (\text{A2})$$

where  $R_{ba}$  is the rate of scattering from an initial state  $a$  to a final state of energy  $\omega_b$ :

$$R_{ba} = \omega_s^3 \alpha_{\text{FS}}^4 \int d\Omega \sum_{s=1,2} \left| \sum_k \frac{(\epsilon_s^* \cdot \mathbf{r}_{bk})(\epsilon \cdot \mathbf{r}_{ka})}{\omega_{ka} \mp \omega} + \frac{(\epsilon \cdot \mathbf{r}_{bk})(\epsilon_s^* \cdot \mathbf{r}_{ka})}{\omega_{kb} \pm \omega} \right|^2 I. \quad (\text{A3})$$

Scattering may proceed via the absorption of a trap photon and emission of a scattered photon of frequency  $\omega_s = -\omega_{ba} + \omega$  (Raman scattering—RS), or via the emission of both a lattice frequency photon and a photon of frequency  $\omega_s = -\omega_{ba} - \omega$  (Singly stimulated two photon emission—SSTPE). The upper signs relate to RS, and the lower signs to SSTPE—which is only possible when  $b$  is lower in energy than  $a$ .

After some straightforward calculations one can re-cast equation (A3) as equation (5) of section 2, where  $r_{bk}$  and  $r_{ka}$  represent radial matrix elements:

$$r_{bk} = \int_0^\infty r^2 dr R_b^*(r) r R_k(r), \quad (\text{A4})$$

$$r_{ka} = \int_0^\infty r^2 dr R_k^*(r) r R_a(r), \quad (\text{A5})$$

with  $R_a(r)$ ,  $R_b(r)$  and  $R_k(r)$  denoting the radial wave function of the corresponding atomic states. The angular term  $\mathcal{A}_{ba}$  includes summation over scattered photon polarisation states, summation over the magnetic quantum number of the final state (the magnetic quantum number of the initial state is 0 here), and integration over the polar angles  $\vartheta$  and  $\varphi$ . The calculation yields  $\mathcal{A}_{ba} = 8\pi/27$  when state  $b$  is an S-state and  $\mathcal{A}_{ba} = 16\pi/27$  when it is a D-state.

We note, in regard to the particular case of Rayleigh scattering, for which  $a = b$ , that equation (4) of section 2 follows immediately from these general results and from equation (3).

## Appendix B. Implicit summation and calculation of radial matrix elements

Calculating the polarisability and scattering rates requires the computation of sums over all atomic states  $k$  that are dipole-coupled to both  $a$  and  $b$ . In principle, this includes a sum over an infinite number of discrete, bound states, and an integration across a continuum of unbound states. Following [51, 62], we carry out this calculation using the implicit summation method (also called the Dalgarno–Lewis method [63, 64]). Here, the sum is replaced by a single matrix element:

$$\sum_k \frac{\epsilon_i \cdot \mathbf{r}_{bk} \epsilon_j \cdot \mathbf{r}_{ka}}{\omega_k - \omega_a \mp \omega} = \langle b | \epsilon_i \cdot \mathbf{r} | \Psi \rangle, \quad (\text{B1})$$

where the subscripts  $i$  and  $j$  simply identify the two polarisation vectors, and the vector  $|\Psi\rangle$  solves the equation

$$[H - (\omega_a \pm \omega)] |\Psi\rangle = \epsilon_j \cdot \mathbf{r} | a \rangle, \quad (\text{B2})$$

where  $H$  is the Hamiltonian including the reduced mass of the system. The vector  $|\Psi\rangle$  includes contributions from both the discrete and continuum parts of the spectrum.

We construct a discrete set of Laguerre functions multiplied by spherical harmonics [65, 66],

$$\mathcal{B} = \left\{ \frac{1}{r} S_{n,l}^{(\zeta)}(r) Y_{lm}(\theta, \phi) : n \in \mathbb{N}, l \in \mathbb{N}_0, |m| \leq l \right\}, \quad (\text{B3})$$

where  $\zeta$  is a free, real parameter. The numbers  $n$  and  $l$  index the Sturmian functions:

$$S_{nl}^{(\zeta)}(r) = \mathcal{N}_{nl} (2\zeta r)^{l+1} e^{-\zeta r} L_{n-1}^{2l+1}(2\zeta r), \quad (\text{B4})$$

with  $\mathcal{N}_{nl}$  a normalising constant.  $L_x^y(s)$  are the associated Laguerre polynomials, expressed in the Rodriguez representation [67].

Such a set of Laguerre functions form a complete set spanning the Hilbert space of  $L^2(0, \infty)$  functions—the space of square integrable functions over the semi-definite interval (see [68] for proof). Thus,  $\mathcal{B}$  forms a complete set spanning the relevant Hilbert space.

We normalise the functions of  $\mathcal{B}$  as  $\mathcal{N}_{nl} = \sqrt{(n-1)!/(n+2l)!}$  such that,

$$\int_0^\infty r^2 dr \left( \frac{1}{r} S_{n'l}^{(\zeta)} \right) \frac{1}{r} \left( \frac{1}{r} S_{nl}^{(\zeta)} \right) = \delta_{n'n}. \quad (\text{B5})$$

Orthogonality over the indexes  $l$  and  $m$  is assured by the orthogonality of the spherical harmonics. This condition, and standard relations between the associated Laguerre polynomials as presented in [67], can be used to analytically evaluate matrix elements of operators. In this way, we produce representations of the Hamiltonian dipole operators in the basis  $\mathcal{B}$ ; we denote these matrices  $\mathcal{H}$  and  $\mathcal{R}$  respectively.

The wave function of an atomic state  $a$  is represented as a vector  $\mathbf{a}$  in the basis  $\mathcal{B}$ . The angular wave functions of hydrogen are given by the same spherical harmonics that give the angular parts of the basis functions  $\mathcal{B}$ . Indeed, the quantum numbers  $l$  and  $m$  relate directly to the indices of the same labels. The radial wave function for atomic state  $a$  with principal quantum number  $N$  can be decomposed over the radial parts of the basis functions:

$$R_{Nl}(r) = \sum_{n \in \mathbb{N}} C_{n,N,l} \frac{1}{r} S_{nl}^{(\zeta)}(r), \quad (\text{B6})$$

where  $C_{n,N,l}$  are constants. We calculate this vector by numerically solving the Schrödinger equation as a generalised eigenvalue problem:

$$\mathcal{H}\mathbf{a} = \omega_a \mathcal{T}\mathbf{a}. \quad (\text{B7})$$

The overlap matrix  $\mathcal{T}$  accounts for the non-trivial overlap between the Sturmian functions.

The calculation of (B1) and (B2) reduces to solving the matrix equation,

$$[\mathcal{H} - (\omega_a \pm \omega) \mathcal{T}] \Psi = \mathcal{R}\mathbf{a}, \quad (\text{B8})$$

and computing the product,

$$\mathbf{b}^T \mathcal{R} \Psi, \quad (\text{B9})$$

for both sums (i) and (ii) independently.

In principle, the choice of  $\zeta$  is free, although convergence is much slower for excessively large values of this parameter. For all calculations presented in this article we let  $n$  range to 300 and set  $\zeta = 0.3$ . We find that this is sufficient to ensure that the resulting values of the scattering rate are stable to 1 part in  $10^9$  under variation to  $\zeta \pm 0.1$ .

The code we use is freely available at [69].

For similar calculations in alkali atoms, it is often sufficient to sum across only a small number of discrete states to converge to the correct value. However, this is not the case in hydrogen, where continuum contributions cannot be neglected. Figure 4 illustrates this point. This figure represents the

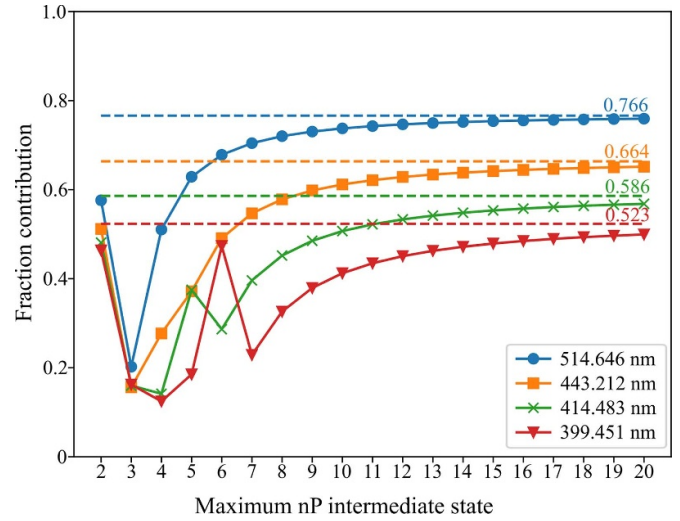


**Figure 4.** The fraction of the total inelastic scattering rate which can be attributed to the lowest  $nP$  intermediate state, summed over  $n$ , for  $n$  varying from 2 to 20. The data points and solid lines show how this fraction increases with  $n$  at the four magic wavelengths considered in this work. The dashed lines represent the convergent limit of this fraction, calculated for a discrete sum up to the 100P state. The difference between this limit and 1 is the contribution of the continuum states.

fraction of the total inelastic scattering rate that is obtained by summing over a finite number of bound intermediate states only. As seen from this figure, failing to consider the continuum contributions to scattering rates underestimates them by 23%–48% at the magic wavelengths. This underestimation increases with photon energy.

### Appendix C. Doppler free spectroscopy in optical traps

In the Doppler free excitation on a two photon transition, the atom experiences two separate momentum kicks in opposing directions. Assuming that the photons come from opposing beams oriented along the lattice axis ( $\hat{x}$ ), the atom experiences two momentum kicks:  $+kx$  and  $-kx$ . The matrix elements for a transition between vibrational states are given:

$$\langle n' | e^{ikx} + e^{-ikx} | n \rangle = \langle n' | e^{i\eta(a^\dagger + a)} + e^{-i\eta(a^\dagger + a)} | n \rangle, \quad (\text{C1})$$

where we have approximated the potential at bottom of a given lattice site as harmonic:  $a$  and  $a^\dagger$  are the ladder operators for the simple harmonic oscillator. The Lamb Dicke parameter  $\eta = \sqrt{E_{\text{probe}}/\omega_T}$  is the ratio between the recoil energy associated with probe photon absorption and the separation of vibrational states.

Expanding (C1) in powers of  $i\eta$ , neglecting higher order terms for small  $\eta$ :

$$\langle n' | 2 + 0 - \eta^2 (a^\dagger + a)^2 + 0 + O(\eta^4) | n \rangle. \quad (\text{C2})$$

Terms with odd powers  $i\eta$  and  $-i\eta$  cancel, while terms with even powers remain. The cancellation of the first order terms

**Table 4.** Fractional SOD shift  $\langle \delta\hat{\nu}/\nu \rangle$  for thermal states in magic wavelength lattices with trap frequencies of 8.79 MHz.

$\lambda/\text{nm}$	$ U_0 /k_B/\text{mK}$	$\bar{n}_{T= U_0 /k_B}$	$\langle \delta\hat{\nu}/\nu \rangle_{T= U_0 /k_B}$	$\bar{n}_{T= U_0 /(3k_B)}$	$\langle \delta\hat{\nu}/\nu \rangle_{T= U_0 /(3k_B)}$
514.6	1.24	2.47	$-5.75 \times 10^{-17}$	0.563	$-2.06 \times 10^{-17}$
443.2	0.919	1.72	$-4.29 \times 10^{-17}$	0.337	$-1.62 \times 10^{-17}$
414.5	0.808	1.46	$-3.79 \times 10^{-17}$	0.264	$-1.48 \times 10^{-17}$
399.5	0.744	1.31	$-3.51 \times 10^{-17}$	0.223	$-1.40 \times 10^{-17}$

is analogous to the elimination of the Doppler shift in field free measurements and here relates to the suppression of first order sidebands.

Constraining consideration to leading order, one finds the probability of transition between vibrational states:

$$P_{n \rightarrow n} = \frac{1}{N} (2 - \eta^2 - 2m\eta^2)^2 \quad (\text{C3})$$

$$P_{n \rightarrow n+2} = \frac{1}{N} \eta^4 (n+1)(n+2) \quad (\text{C4})$$

$$P_{n \rightarrow n-2} = \frac{1}{N} \eta^4 (n)(n-1), \quad (\text{C5})$$

where  $N$  is some normalising function such that  $\sum_{n'} P_{n \rightarrow n'} = 1$  for all vibrational states  $n'$ . Transitions  $n \rightarrow n$  contribute to the central carrier signal, whilst transitions  $n \rightarrow n \pm 2$  contribute to second order sidebands and are detuned from the carrier by  $\pm 2\nu_T$ .

### C.1 The second order Doppler shift

Following the arguments of [53], one obtains the following relativistic shift to the probe frequency in the atom frame:

$$\left\langle \frac{\delta\hat{\nu}}{\nu} \right\rangle_n = -\frac{h\nu_T}{4m_{\text{H}}c^2} (2n+1) - \left( \frac{g}{2\pi\nu_T c} \right)^2 + \frac{\phi_0}{c^2}. \quad (\text{C6})$$

where  $g$  is the acceleration due to gravity in the measurement direction and  $\phi_0$  is the gravitational potential at the centre of a given lattice site. The first term is the frequency shift from the second-order Doppler (SOD) effect whilst the second and third terms describe gravitational red-shift. The gravitational red-shift terms are negligible compared to the SOD term,  $O(10^{-29})$  compared to  $O(10^{-17})$ , so we have:

$$\left\langle \frac{\delta\hat{\nu}}{\nu} \right\rangle_n = -\frac{h\nu_T}{4m_{\text{H}}c^2} (2n+1). \quad (\text{C7})$$

Consider frequency shifts in an optical potential with trap frequency 8.79 MHz (as in table 3). For  $n=0$  we obtain a fractional shift of  $-9.68 \times 10^{-18}$ .

The shift in a thermal state at temperature  $T$  can be found by replacing  $n$  in equation (C7) with the average occupation number:

$$\bar{n} = \frac{1}{\exp\left(\frac{h\nu_T}{k_B T}\right) - 1}, \quad (\text{C8})$$

where  $k_B$  is the Boltzmann constant.

The lattices described in table 3 have depths  $|U_0|/k_B O(1)$  mK. Table 4 contains the SOD shift for thermal states with temperature  $T = |U_0|/k_B$  and  $T = |U_0|/(3k_B)$  in each magic wavelength lattice. The shallow traps and large trap frequencies lead to low average occupations  $\bar{n}$ , so thermal state shifts remain small.

### ORCID iDs

J P Scott  <https://orcid.org/0000-0002-1282-1610>

R M Potvliege  <https://orcid.org/0000-0003-4624-1064>

D Carty  <https://orcid.org/0000-0002-1598-9021>

M P A Jones  <https://orcid.org/0000-0003-1514-5977>

### References

- [1] Karshenboim S G 2010 *Phys. Rev. Lett.* **104** 220406
- [2] Brax P and Burrage C 2011 *Phys. Rev. D* **83** 035020
- [3] Stadnik Y V 2018 *Phys. Rev. Lett.* **120** 223202
- [4] Jones M P A, Potvliege R M and Spannowsky M 2020 *Phys. Rev. Res.* **2** 013244
- [5] Delaunay C, Karr J-P, Kitahara T, Koelemeij J C, Soreq Y and Zupan J 2023 *Phys. Rev. Lett.* **130** 121801
- [6] Alexandrou C, Hadjiyiannakou K, Koutsou G, Otnad K and Petschlies M 2020 *Phys. Rev. D* **101** 114504
- [7] Parthey C G et al 2011 *Phys. Rev. Lett.* **107** 203001
- [8] Matveev A et al 2013 *Phys. Rev. Lett.* **110** 230801
- [9] Xiong W and Peng C 2023 *Universe* **9** 182
- [10] Tiesinga E, Mohr P J, Newell D B and Taylor B N 2021 *Rev. Mod. Phys.* **93** 025010
- [11] Mohr P J, Newell D B and Taylor B N 2016 *J. Phys. Chem. Ref. Data* **45** 043102
- [12] Pohl R, Gilman R, Miller G A and Pachucki K 2013 *Annu. Rev. Nucl. Part. Sci.* **63** 175
- [13] Gao H and Vanderhaeghen M 2022 *Rev. Mod. Phys.* **94** 015002
- [14] Brandt A D, Cooper S F, Rasor C, Burkley Z, Matveev A and Yost D C 2022 *Phys. Rev. Lett.* **128** 023001
- [15] Fleurbaey H, Galtier S, Thomas S, Bonnaud M, Julien L, Biraben F m c, Nez F M C, Abgrall M and Guéna J 2018 *Phys. Rev. Lett.* **120** 183001
- [16] Grinin A, Matveev A, Yost D C, Maisenbacher L, Wirthl V, Pohl R, Hansch T W and Udem T 2020 *Science* **370** 1061
- [17] Bezginov N, Valdez T, Horbatsch M, Marsman A, Vutha A C and Hessels E A 2019 *Science* **365** 1007
- [18] Beyer A et al 2017 *Science* **358** 79
- [19] Schwob C, Jozefowski L, de Beauvoir B, Hilico L, Nez F, Julien L, Biraben F, Acef O, Zondy J-J and Clairon A 1999 *Phys. Rev. Lett.* **82** 4960
- [20] de Beauvoir B, Nez F, Julien L, Cagnac B, Biraben F, Touahri D, Hilico L, Acef O, Clairon A and Zondy J J 1997 *Phys. Rev. Lett.* **78** 440
- [21] de Beauvoir B, Schwob C, Acef O, Jozefowski L, Hilico L, Nez F, Julien L, Clairon A and Biraben F 2000 *Eur. Phys. J. D* **12** 1434
- [22] Derevianko A and Katori H 2011 *Rev. Mod. Phys.* **83** 331

- [23] Takamoto M, Hong F-L, Higashi R and Katori H 2005 *Nature* **435** 321
- [24] Le Targat R, Baillard X, Fouché M, Bruschi A, Tcherbakoff O, Rovera G D and Lemonde P 2006 *Phys. Rev. Lett.* **97** 130801
- [25] Ludlow A D, Boyd M M, Zelevinsky T, Foreman S M, Blatt S, Notcutt M, Ido T and Ye J 2006 *Phys. Rev. Lett.* **96** 033003
- [26] Barber Z W, Hoyt C W, Oates C W, Hollberg L, Taichenachev A V and Yudin V I 2006 *Phys. Rev. Lett.* **96** 083002
- [27] Bothwell T, Kedar D, Oelker E, Robinson J M, Bromley S L, Tew W L, Ye J and Kennedy C J 2019 *Metrologia* **56** 065004
- [28] Crivelli P and Kolachevsky N 2020 *Hyperfine Interact.* **241** 1
- [29] Shore G M 2005 *J. Nucl. Phys. B* **717** 86
- [30] Kostelecky V A and Vargas A J 2015 *Phys. Rev. D* **92** 056002
- [31] Ahmadi M et al 2017 *Nature* **541** 506
- [32] Ahmadi M et al 2018 *Nature* **557** 71
- [33] Adhikari C M, Kawasaki A and Jentschura U D 2016 *Phys. Rev. A* **94** 032510
- [34] Adhikari C M, Canales J C, Arthanayaka T P and Jentschura U D 2022 *Atoms* **10** 1
- [35] Zernik W 1964 *Phys. Rev.* **133** A117
- [36] Heno Y, Maquet A and Schwarcz R 1980 *J. Appl. Phys.* **51** 11
- [37] Klarsfeld S 1972 *Phys. Rev. A* **6** 506
- [38] Zernik W 1964 *Phys. Rev.* **135** A51
- [39] Rapoport L P, Zon B A and Manakov L P 1969 *Sov. Phys. JETP* **29** 220
- [40] Gontier Y and Trahin M 1971 *Phys. Rev. A* **4** 1896
- [41] Khristenko S V and Vetchinkin S I 1976 *Opt. Spectrosc.* **40** 3 (Engl. Transl.)
- [42] Karule E and Moine B 2003 *J. Phys. B: At. Mol. Opt. Phys.* **36** 1963
- [43] Drake G (ed) 2006 *Springer Handbook of Atomic, Molecular and Optical Physics* 2nd edn (Springer)
- [44] Grimm R, Weidemüller M and Ovchinnikov Y B 2000 *Advances in Atomic, Molecular and Optical Physics* vol 42 (Elsevier) pp 95–170
- [45] Haas M, Jentschura U D and Keitel C H 2006 *Am. J. Phys.* **74** 77
- [46] Le Kien F, Schneeweiss P and Rauschenbeutel A 2013 *Eur. Phys. J. D* **67** 1
- [47] Dörscher S, Schwarz R, Al-Masoudi A, Falke S, Sterr U and Lisdat C 2018 *Phys. Rev. A* **97** 063419
- [48] Alnis J, Matveev A, Kolachevsky N, Udem T and Hänsch T W 2008 *Phys. Rev. A* **77** 053809
- [49] Bräunlich P and Lambropoulos P 1970 *Phys. Rev. Lett.* **25** 135
- [50] Gavrilin M 1979 *Z. Phys. A* **293** 269
- [51] Potvliege R 1998 *Comput. Phys. Commun.* **114** 42
- [52] Biraben F, Julien L, Plon J and Nez F 1991 *Europhys. Lett.* **15** 831
- [53] Martínez-Lahuerta V, Eilers S, Mehlstäubler T, Schmidt P and Hammerer K 2022 *Phys. Rev. A* **106** 032803
- [54] Gabrielse G et al 2018 *Opt. Lett.* **43** 2905
- [55] Jitrik O and Bunge C F 2004 *J. Phys. Chem. Ref. Data* **33** 1059
- [56] Vliegen E, Hogan S D, Schmutz H and Merkt F 2007 *Phys. Rev. A* **76** 023405
- [57] Seiler C, Agner J A, Pillet P and Merkt F 2016 *J. Phys. B: At. Mol. Opt. Phys.* **49** 094006
- [58] Potvliege R M, Nicolson A, Jones M P and Spannowsky M 2023 *Phys. Rev. A* **108** 052825
- [59] Vázquez-Carson S F, Sun Q, Dai J, Mitra D and Zelevinsky T 2022 Direct laser cooling of calcium monohydride molecules *New J. Phys.* **24** 083006
- [60] Udem T 2023 private communication
- [61] Loudon R 2010 *The Quantum Theory of Light* 3rd edn (Oxford University Press)
- [62] Potvliege R and Shakeshaft R 1989 *Z. Phys. D* **11** 93
- [63] Mavromatis H A 1991 *Am. J. Phys.* **59** 738
- [64] Nandi T, Bera P, Panja M and Talukdar B 1996 *J. Phys. A: Math. Gen.* **29** 1101
- [65] Hostler L C 1970 *J. Math. Phys.* **11** 2966
- [66] Maquet A, Vénier V and Marian T A 1998 *J. Phys. B: At. Mol. Opt. Phys.* **31** 3743
- [67] Gradshteyn I S and Ryzhik I M 2015 *Table of Integrals, Series and Products* 8th edn (Academic)
- [68] Szegő G 1939 *Orthogonal Polynomials* 1st edn (American Mathematical Society)
- [69] Scott J P 2023 Hydrogen-s-state-2-photon(1.0) (<https://doi.org/10.5281/zenodo.10034256>)